Electronic Supplementary Material (ESI) for Journal of Materials Chemistry C.


# Supporting Information

## Freestanding $CH_3NH_3PbBr_3$ Single-crystal Microwires for Optoelectronic Applications Synthesized with a Predefined Lattice Framework

Figure S1 shows the schematic diagram of the two processes for synthesizing $PbBr_2$ milliwires and microwires, respectively. With antisolvent slowly diffusing into the $PbBr_2$/DMF solutions, the solute will slowly nucleate. If there is no magneton rotating in the solution, the number of nuclear formed in the solution is relatively small. And then the remaining solution will continue to crystallize with these nuclear as the growth origin to form large sized milliwires. In contrast, the static growth environment will be broken if there is a magneton stirring in the solution, resulting in a sharp increase in nucleation points. As result, the remaining solution will crystalize with these nucleation points and form a large number of tiny microwires. Therefore, the size of the $PbBr_2$ microwires can be controlled in the range of micrometers to millimeters by controlling the number of nucleation points.

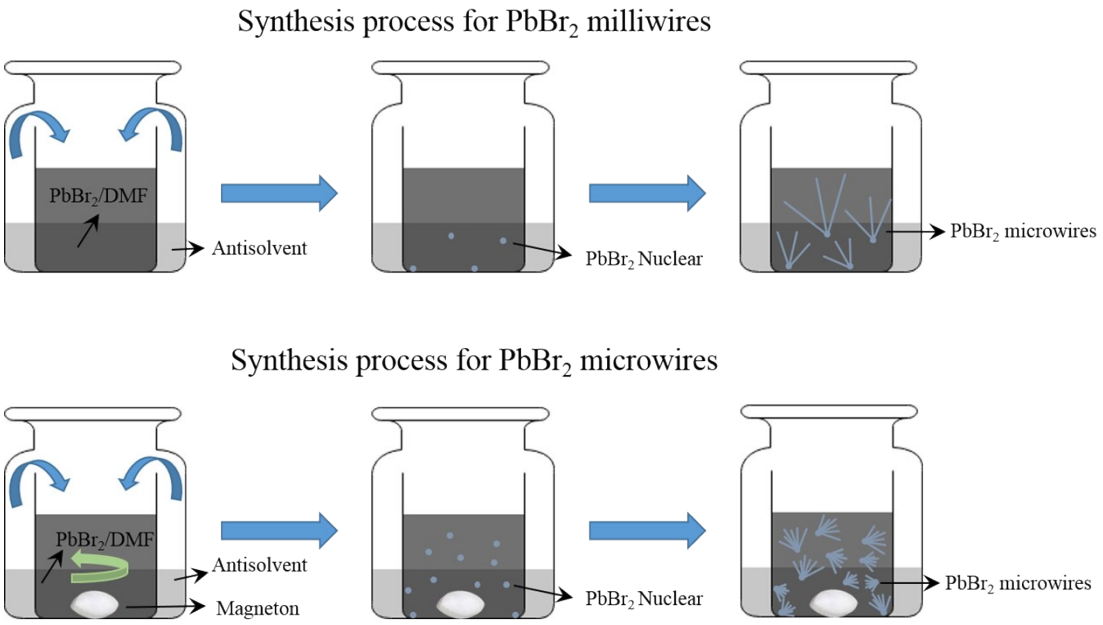


**Figure S1.** Schematic illustration of the antisolvent process to fabricate large sized $PbBr_2$ milliwires and small sized $PbBr_2$ microwires.

Figure S2 shows the $PbBr_2$ microwires before and after reaction with MABr/FABr/CsBr isopropanol solution. It is clearly observed that the color change from white to their corresponding colors after the reaction, indicating the conversion from $PbBr_2$ to perovskite microwires is effective. Moreover, the high density of microwires in the bottle proves the high yield of the novel synthesis method.

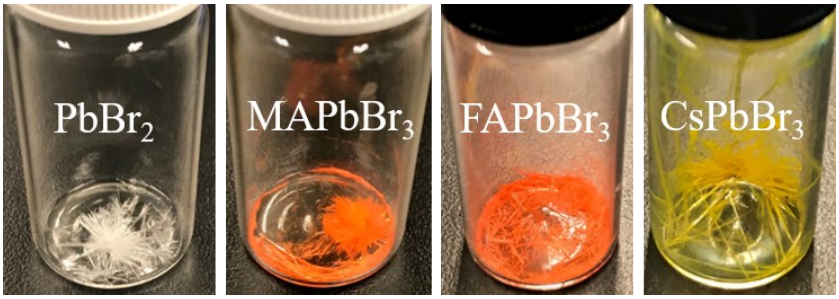


**Figure S2.** Optical image of high yield large dimensions $PbBr_2$ microwires and transformed perovskite microwires.

Figure S3 shows scanning electron microscopy images of the surface and cross section of the large-sized $MAPbBr_3$ microwire, which indicates the smooth surface except for residual particles adhered to the surface. In addition, C, Pb, Br elements evenly distributed on the surface of the cross-

section direction and quantitative elemental analysis yields an average Br/Pb ratio of 2.9, which indicates the effective conversion from $PbBr_2$ to $MAPbBr_3$ microwires.

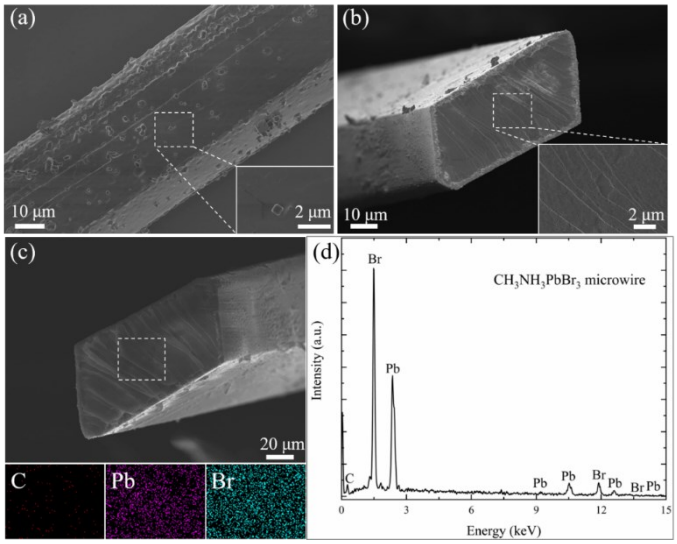


**Figure S3.** (a-b) Top-view and cross-section SEM of single $MAPbBr_3$ microwire, respectively. insets: local magnification images; (c) C, Br, and Pb element mapping images for the cross section of $MAPbBr_3$ microwire. (d) A representative EDX spectrum from (c) and quantitative elemental analysis yields an average Br/Pb ratio of 2.9.

As the framework of perovskite, the octahedral structure of $PbBr_2$ can be converted into not only methylamine perovskite microwires, but also other monovalent cation perovskites. The high crystal quality $PbBr_2$ microwires will be transformed into $FAPbBr_3$ or $CsPbBr_3$ microwires when immersing them in FABr or CsBr isopropanol solution. Figure S4a-b display the SEM images of converted $FAPbBr_3$ and $CsPbBr_3$ microwires. The surface of the microwire is smooth except for some residual particles, which indicates its good crystal quality. To prove whether the $PbBr_2$ microwires were successfully transformed to corresponding perovskite microwires, the PL spectra of the microwires under 473 nm excitation were performed (Figure S4c-d). The center emission peak of the $FAPbBr_3$ microwire is 541 nm (2.29 eV), which is consistent with the band gap of 2.26 eV ($FAPbBr_3$ nanowires) in the previous report[1]. In addition, the emission peak of $CsPbBr_3$ microwire is 525 nm (2.36 eV), which agrees well with the band gap of 2.34 eV ($CsPbBr_3$

nanowires) in the previous report[2]. As a result, the single crystal $PbBr_2$ microwires were successfully transformed into $FAPbBr_3$ and $CsPbBr_3$ microwires.

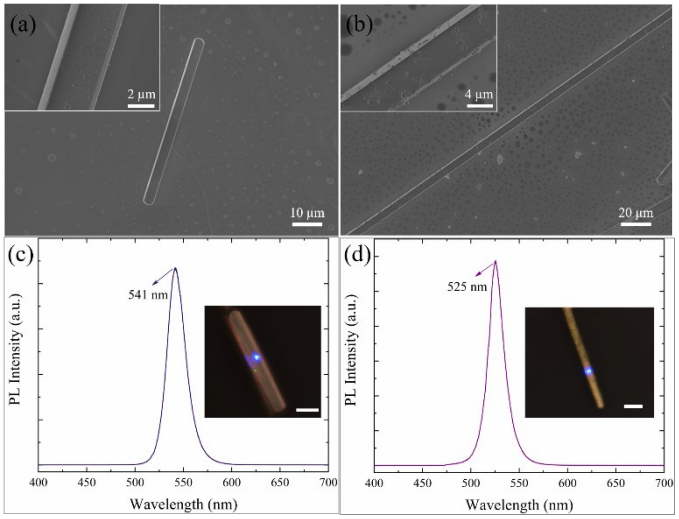


**Figure S4.** (a, b) Top-view SEM images of single $FAPbBr_3$ and $CsPbBr_3$ microwire, respectively; Insets: Partial magnification of the corresponding microwire's surface. (c, d) PL spectra of $FAPbBr_3$ and $CsPbBr_3$ microwires under 473 nm excitation, respectively. Scale bar: 10 μm.

Table 1 FWHM of comparison between $CH_3NH_3PbBr_3$ single crystal and microwire XRD peak

| | | $CH_3NH_3PbBr_3$ single crystal | Single $CH_3NH_3PbBr_3$ microwire |
|---|---|---|---|
| 001 | Kα1 | $0.073^0$ | $0.019^0$ |
| | Kα2 | $0.035^0$ | $0.036^0$ |
| 002 | Kα1 | $0.022^0$ | $0.036^0$ |
| | Kα2 | $0.017^0$ | $0.019^0$ |

Figure S5 shows the evolution from $PbBr_2$ microwires to $MAPbBr_3$ microwires with XRD characterization. With increasing the immersing time, all the peaks of $PbBr_2$ vanished but the peaks of MAPbBr3 gradually emerge and dominate until all the peaks of $PbBr_2$ eliminate, implying that $PbBr_2$ was completely converted into $MAPbBr_3$. The conversion process from $PbBr_2$ to $MAPbBr_3$ indicates the fast ion diffusion of $MA^+$ and $Br^-$ into the crystal lattice of $PbBr_2$.

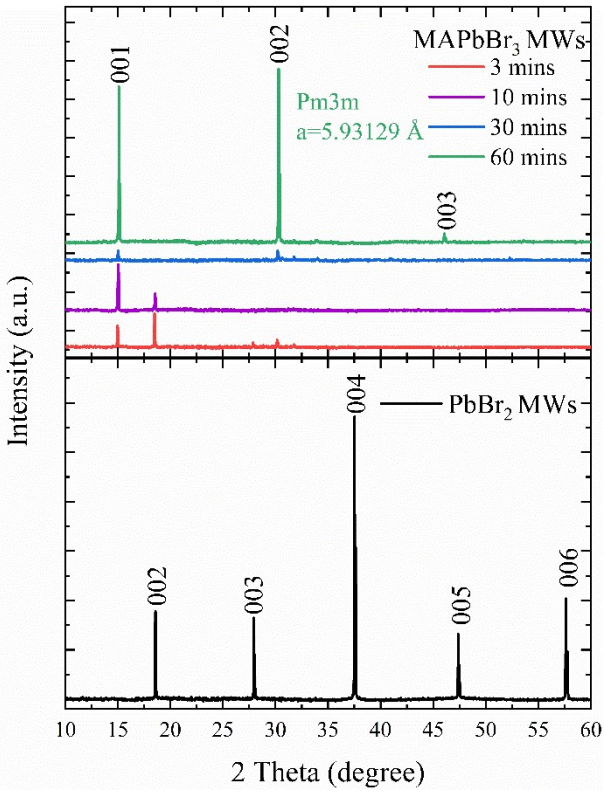


**Figure S5.** X-ray patterns of the conversion process from $PbBr_2$ to $MAPbBr_3$ microwires with different dipping time, the patterns are carried out on a 60 microns diameter single wire.

Figure S6 shows the carrier lifetime of the single crystal obtained according to the traditional direct antisolvent synthesis method. From the inset, we can observe that the microplates and microwires exist simultaneously in the growth process, which may be caused by the uneven diffusion of the anti-solvent into the source solution during the crystallization process. In addition, the carrier lifetime of the microplates/microplates have a fast and slow time component 3.7 ns, 97.4 ns, respectively.

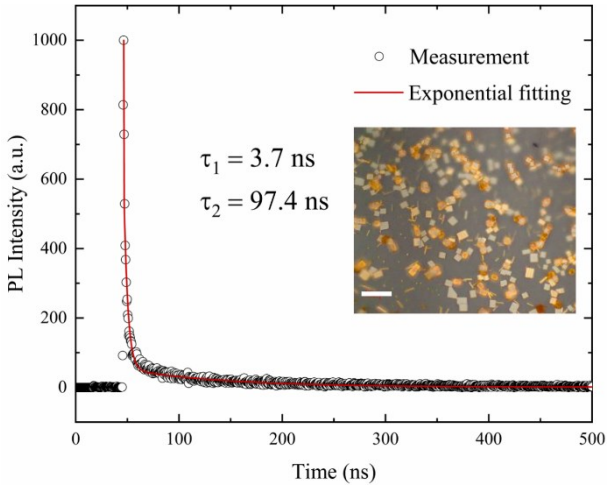


**Figure S6.** TRPL decay spectrum of $MAPbBr_3$ single crystal, with bi-exponential fitting parameter of fast (3.7 ± 0.11 ns) and slow (97.4 ± 1.57 ns) transient. The inset shows the as-prepared singe crystal sample. Scale bar: 50 μm.

In order to illustrate the high speed of the single $MAPbBr_3$ microwire's carrier migration, the single-carrier device was fabricated, as shown in the inset of Figure S7. The small single microwire with a diameter of about 2.8 μm was placed on the substrate which was act as an electrode with a trench. In addition, the single microwire was tightly attached to both ends of the electrode with an interval of about 30 μm. The carrier mobility of the single microwire-based photodetector could be calculated with Mott-Gurney law:[3]

$$J = \frac{9\varepsilon\varepsilon_0\mu V^2}{8d^3}$$

where V is the applied voltage, ε (=25.5 [4]) is the relative dielectric constant of $MAPbBr_3$ and $\varepsilon_0$ is the vacuum permittivity, d is the spacing between the electrodes, and μ is the carrier mobility of the device. The mobility can be calculated with the slope of $J^{1/2}/V$ as about 36 $cm^2\ V^{-1}\ s^{-1}$, which is close to the previous report 38±5 $cm^2\ V^{-1}\ s^{-1}$ of $MAPbBr_3$ bulk single crystal[5]. This result shows the superior carrier mobility of the microwire similar to a bulk single crystal.

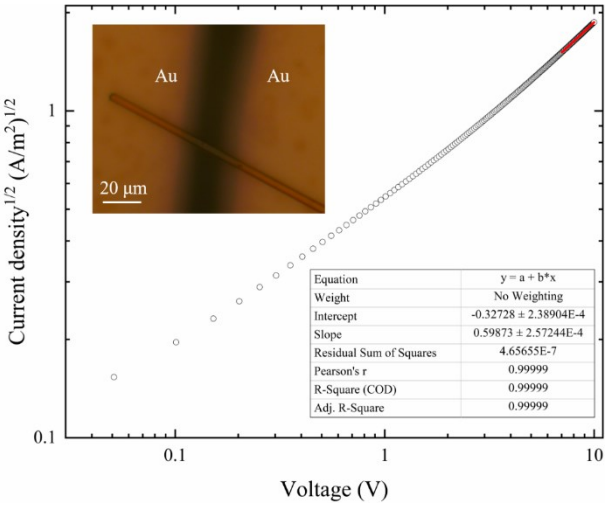


**Figure S7.** The current density$^{1/2}$ – Voltage bias ($J^{1/2}$ - V) curves of the single microwire-based photodetector.

Figure S8 shows the photo-switching behavior under 450 nm light irradiation with different voltage bias. The light response with time indicates that the sensitivity to incident light is highly stable and repeatable. In addition, the photocurrent decreases monotonously with the decrease of the bias voltage, which is reasonable, because a large electric field can promote the effective transport of photocarriers and reduce their probability of recombination.

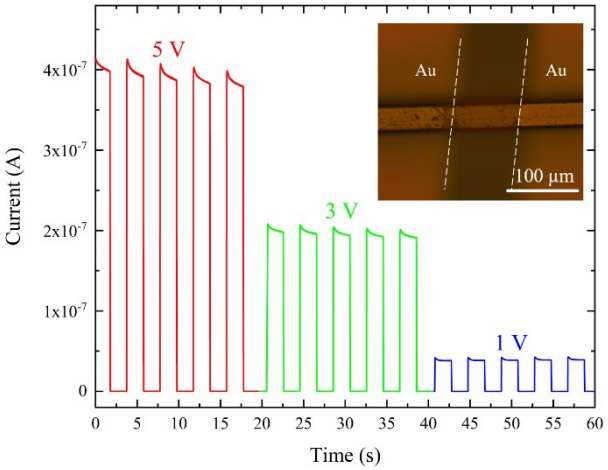


**Figure S8.** Time-dependent photo-switching behavior under 450 nm light irradiation with different voltage bias; Insets: the optical image of the photodetector.

The LDR of a photodetector is the maximum linear response divided by the detector noise and it will eventually appear as non-linear as the irradiation power increase to an upper point. The LDR

is usually calculated by the following formula:

$$LDR = 20 \times log\frac{P_{max}}{P_{min}}$$

where $P_{max}$ and $P_{min}$ represent the upper and lower limits of the illumination power.

The responsivity measures the input-output gain of the detector system. In the specific case of photodetectors, responsivity measures the electrical output of each light input. And the responsivity of a photodetector is usually expressed in amperes or volts per watt of incident radiation power, which can be calculated from EQE according to the equation:

$$R = \frac{EQE}{hc/\lambda q}$$

where $h$ is Plank constant, $c$ is the velocity of light, $\lambda$ is the light wavelength. This equation reveals that the responsivity curves have a similar shape with EQE.

Figure S9 shows the detectivity of the photodetector under 5 V, and the detectivity behaves a similar shape with the absorption spectrum. This device shows obvious detection ability for light in the range of 300-550 nm and reaches a maximum value of $1.4\times10^9$ cm $Hz^{1/2}$ $W^{-1}$ at 530 nm.

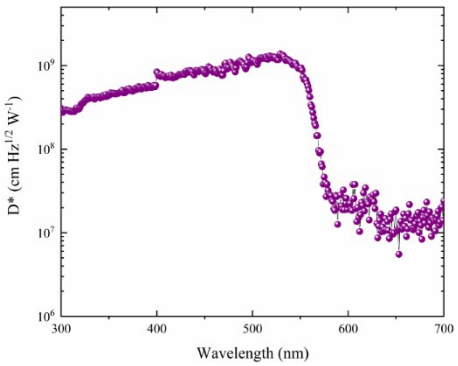


**Figure S9.** The specific detectivity of the photodetector under 5 V bias calculated from responsivity spectrum.

Figure S10 shows the comparation between photocurrent and displacement under different light power densities. There is a clear difference of photocurrent under the white point source irradiation with/without thread, indicating the photocurrent was effectively affected by the barrier.

In addition, the change of the photocurrent will be more obvious under stronger light irradiation, which could be attributed to better suppression of noise under high light intensity. In addition, the fitting of the barrier-free light response behaves fine Gaussian distribution, which shows that the single microwire-based photodetector has a certain potential in light intensity detection.

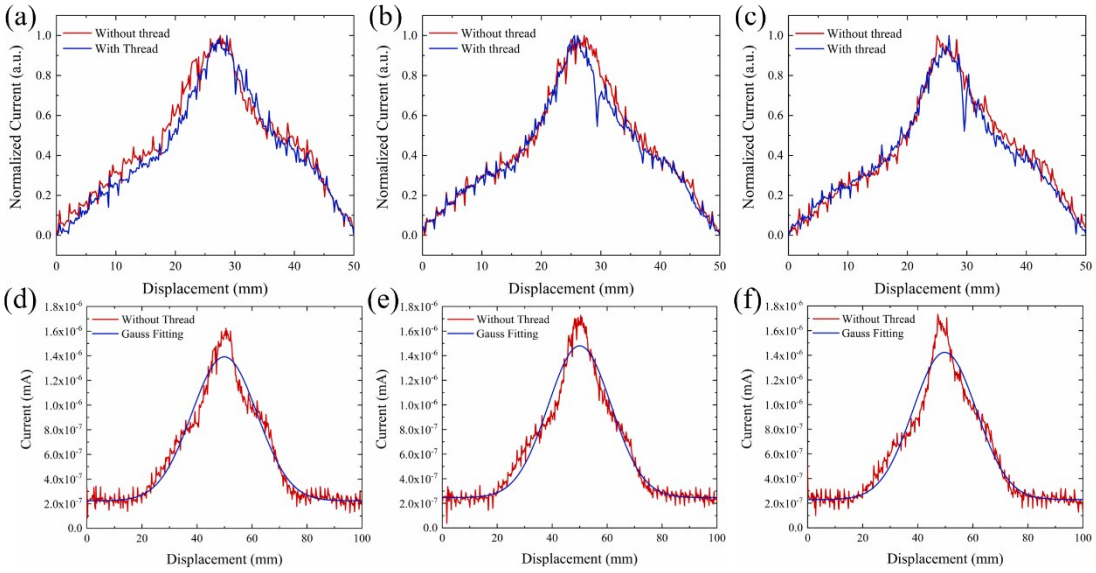


**Figure S10.** (a-c) The relationship between light response and distance under different light power densities 8 mW/cm$^2$, 9 mW/cm$^2$, 10 mW/cm$^2$, respectively. (d-f) The Gaussian fitting of the above barrier-free light response.

In addition, as shown in Figure S11, we have established a simple blue light communication system based on the perovskite micro-wire single crystal, demonstrating its application potential in visible light communication (VLC). As an emerging communication technology, VLC has broadened the communication spectrum to a certain extent and has shown broad application prospects in the fields of home interconnection, rail transit, and terrain surveying. Among them, the blue light communication technology has the advantages of high energy efficiency, low power consumption, high confidentiality, etc., and has great application potential in special environments such as underwater communication. As shown in Figure S11a, the blue light communication system consists of two parts: signal generation and signal reception. In the signal generation part, the

instructions output by the computer are converted into high- and low-level signals by the driver Stm32F407 to control the operation of the 450 nm LED light. Among them, the data 1/0 represents the high/low level of the transmission and the light/darkness of the LED light. In the signal receiving part, under the bias voltage of +15 V, the current response of the perovskite micro-wire single crystal to the blue LED is obtained by Keithley 2601 under the control of computer software. In order to more clearly show the accuracy and stability of the data in the transmission process of the system, Figure S11b shows a comparison diagram of signal generation and reception. It can be seen that there is no obvious distortion in data transmission in the system, which shows that our equipment is in a good and stable operating state. On this basis, we believe that after further development in software, our devices can complete the transmission of audio, text and other data, and provide new detection devices for the development of blue light communication technology.

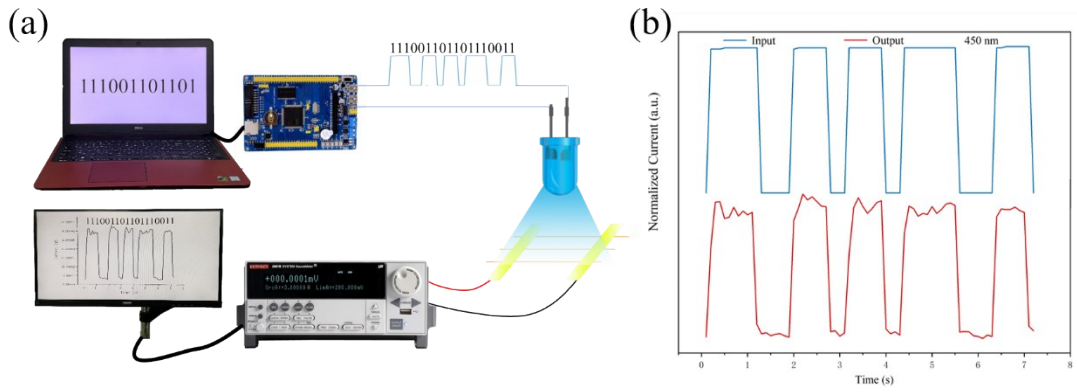


**Figure S11.** (a) Schematic of blue light communication system based on the perovskite single crystal microwire. (b) Comparation diagram of signal generation and reception.

**References**

1. Y. Fu, H. Zhu, A. W. Schrader, D. Liang, Q. Ding, P. Joshi, L. Hwang, X. Y. Zhu and S. Jin, *Nano Lett.*, 2016, **16**, 1000-1008.

2. M. Shoaib, X. Zhang, X. Wang, H. Zhou, T. Xu, X. Wang, X. Hu, H. Liu, X. Fan, W. Zheng, T. Yang, S. Yang, Q. Zhang, X. Zhu, L. Sun and A. Pan, *J. Am. Chem. Soc.*, 2017, **139**, 15592-15595.

3. Q. Dong, Y. Fang, Y. Shao, P. Mulligan, J. Qiu, L. Cao and J. Huang, *Science*, 2015, **347**, 967-970.

4. A. Poglitsch and D. Weber, *J. Chem. Phys.*, 1987, **87**, 6373-6378.

5. D. Shi, V. Adinolfi, R. Comin, M. Yuan, E. Alarousu, A. Buin, Y. Chen, S. Hoogland, A. Rothenberger and K. Katsiev, *Science*, 2015, **347**, 519-522.